Trailing Edge Slope Ocean Wind Speed Retrievals Using CYGNSS's Full DDMs

Stephen J. Katzberg , Mohammad Al-Khaldi , *Member, IEEE*, Faozi Said ,
and Jeonghwan Park , *Member, IEEE*

Abstract—The launch of the CYGNSS constellation in 2016 represents NASA's first mission dedicated to the acquisition of GPS signals reflected off the earth's surface. The major geophysical measurement objective is ocean surface winds with particular emphasis placed on the improved characterization of tropical cyclones. The conventional method for retrieving ocean surface winds using spaceborne Global Navigation Satellite System Reflectometry systems, of which CYGNSS is one example, is to measure the reflected power from the specular point on the ocean surface. Accurate measurement of surface power is complicated by calibration of the various power levels from the transmitting satellites, geometric effects, receiving system RF chain characteristics, among others. This article applies an alternative trailing edge slope (TES) method, which is more immune to end-to-end calibration uncertainties. It is nonetheless noted that because TES is a fundamentally shape-based measure of the waveform, it is susceptible to factors that may distort the measurements' slopes. This included measurements made with low SNR (on the order of 1.5 dB or less) due to low level of surface scattering or observations within the low gain portion of the receive antenna pattern. For this reason, in this work retrieval attempts are largely limited to those with a receive gain on the order of 10 dB or better. The TES method is based on the slope of the measured signal as a function of delay. Given the need for a delay space that extends beyond the $\approx$2.5–3.5 chips provided by CYGNSS's standard Level-1 measurements, its utility is explored using one of the constellation's special "full DDM" downlink modes. The TES method is shown to provide competitive retrievals including measurements from the surface, where the conventional method provides ocean wind speed estimates of lower accuracy. Tradeoffs using the TES method are discussed as well as simple improvements in the method are given. It is also noted that because with TES, measurements' slopes are the fundamental observable no calibration of measurements is required.

Index Terms—Microwave remote sensing, ocean winds, spaceborne GNSS-R.

I. INTRODUCTION

THE monitoring of ocean surface winds in support of various meteorological forecasting along with cyclonic development and propagation inland monitoring activities using spaceborne sensors has had a long history of investigation beginning with the TIROS-3 satellite [1] in 1961 and evolving over time to more mature systems like Advanced SCATerometer (ASCAT-A) first launched in 2006 and later followed by the "B" and "C" satellites [2], [3], [4]. The increased reliance on spaceborne observatories for providing accurate ocean surface winds is motivated, to a large extent, by their global coverage. This in turn enables more comprehensive monitoring and characterization of surface conditions.

Traditional spaceborne sensors are nonetheless associated with known limitations some of which relate to the impacts of higher rain rates, leading to increased attenuation of impinging and reflected signals, relied upon in the sensing process, thereby compromising their ability to accurately characterize surface conditions. Cloud covers pose a similar limitation.

On the other hand, L-band microwave spaceborne remote sensing of the Earth's surface offer an effective complementary means for a similar set of applications.

Of particular interest is the use of Global Navigation Satellite System Reflectometry (GNSS-R) systems [5], [6], [7], [8] for this purpose owing to the ability to deploy fleets of these observatories at a reduced cost given their construction from commercially available components along with their passive mode of operation. In turn, their more dense coverage provides finer temporal sampling thereby increasing the visibility of dynamic change particularly over surface properties undergoing rapid change [9].

The suitability of these systems for the continuous monitoring of the Earth's surface is further aided by their operation within the L-band such that received reflections are less sensitive to the confounding effects of dense vegetation, heavy rain, and cloud cover [10] thereby expanding their utility across scenes typically opaque when observed using higher frequency platforms. Combined, these factors have materialized in the ability to use spaceborne GNSS-R observatories for a swath of disparate applications as demonstrated using measurements made by NASA's 2016 Earth Venture Cyclone Global Navigation Satellite System (CYGNSS) Mission [11], [12].

It is noted that while this work is intended to demonstrate the feasibility of TES retrievals using CYGNSS's full
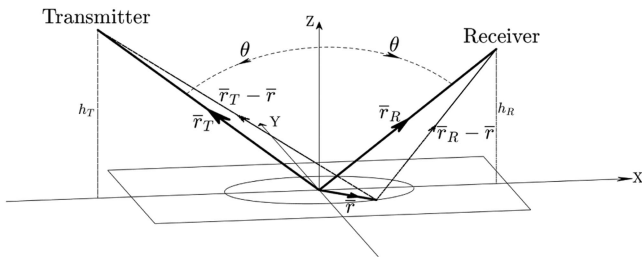
Fig. 1.   Illustration of specular bistatic geometry.

delay-Doppler Map (DDM) downlinks, future investigations intended to transition this approach to operations are encouraged to pursue a more rigorous analysis of the effects of specific observation scenarios, SNR effects, delay cutoffs, impacts the Earth's curvature and given a larger pool of measurements over "fully developed" ocean scenes. For simplicity, analysis here is largely limited to high quality observations made with a receive gain of 10 dBs or better.

The next section overviews the underpinning of the fundamental GNSS-R "delay-Doppler Map" measurements, the relevant data products provided by the CYGNSS mission, processing of the received signal and major limitations associated with the standard "geophysical model function" retrieval approaches. Section II-C provides descriptions of power versus delay trailing edge slopes as a function of the ocean's bivariate Gaussian slope probability density function (SPDF) and highlights how such "shape based" techniques, previously explored and applied in numerous works [6], [13], [14], [16], [17], [18], [19], may provide estimates that are less sensitive to calibration uncertainties. Example results, highlighting the efficacy of trailing edge slope methods applied to a multihour CYGNSS special "full DDM" collection, are explored in Section III. Discussion of retrieval results and recommendations for future work are included in Section IV. Finally, Section V concludes this article.

II. BACKGROUND

A. Fundamental GNSS-R Operation

The typical GNSS-R geometry is depicted in Fig. 1, comprising a GNSS-R receiver, a GNSS transmitter and a reflecting surface, where θ is the incidence and scattering angles, $\bar{r}_T$ is the radial vector between specular point and transmitter, $\bar{r}_R$ is the radial vector between specular point and receiver, $\bar{r}$ is the radial vector between specular point and an arbitrary surface point, $\bar{h}_T$ is the height of transmitter above the plane tangential to the surface, and $\bar{h}_R$ is the height of receiver above the plane tangent to the Earth's surface at the specular point.

GNSS-R geometries are bistatic specular geometries in which the incidence θ_i and scattering θ_s angles are equal ($\theta_i = \theta_s = \theta$) with an azimuthal angular separation ϕ of $180°$. The specular point is the reflecting surface point that gives rise to a minimum in total propagation distance of the signal as it is transmitted by a Global Navigation Satellite System (GNSS), reflected off the Earth's surface and received by the GNSS-R receiver. GNSS-R observatories are therefore "passive" radars that do not transmit signals and instead rely on available Earth reflections of GNSS

transmissions as part of their "opportunistic" mode of remote sensing.

The observed surface is typically "roughened" by either topographic profiles within the measurement's footprint, as is the case with specular points over land, or by a forcing phenomena like surface wind [7], [8], as is the case with ocean surfaces. The observed surface can be thought of as comprising randomly oriented scattering facets each with a height and tilt. Depending on the orientation of each of the facets, some will scatter power toward the receiver and others will scatter power in random directions. The surface area contributing to the bulk of the signal scattering toward the receiver is known as the glistening zone [6], [19]. Its size is dictated in large by the observed surface's levels of roughness. The rougher the surface is, the larger the glistening zone is expected to be; proportionally less power is reflected from the immediate vicinity of the specular point and more power is scattered toward the receiver from points farther away. Conversely, the smoother the surface is, the smaller the glistening zone is expected to be where the bulk of the signal received is expected to have been scattered from the specular point and the small area surrounding it. The properties of the received signal are therefore highly contingent on the properties of the scattering surface, but are also complicated by the characteristics of the receiver, explored further in Sections II-B and II-C.

It is important to note however that in contrast to a traditional "point target" observation scenario in which a radar expects a single dominant reflection, with GNSS-R the target is a large footprint off which multiple "echoes" or reflections are expected. Each reflection is expected to be associated with a delay τ and Doppler f_D. In the context of GNSS-R, delay diversity arises due to the varied "off-specular" paths scattered signals taken from the different surface points within the measurement's footprint. Delay and Doppler solutions for an example spaceborne observation geometry are depicted in Fig 2(a). They highlight the variability of τ and f_D solutions across the region surrounding the specular point with τ estimates progressively increasing, relative to the specular point, due to the increase in forward propagation distances from the transmitter to the reflecting surface point and from there onto the GNSS-R receiver. Similar increases in f_D are noted due to relative velocity drifts.

This delay-Doppler variability enables partitioning the received power into different "bins" such that the basic measurement operation is that of mapping power from the spatial domain to an equivalent 2-D delay-Doppler space to form the fundamental GNSS-R measurement, DDM depicted in Fig. 2(b) as indicated by the corresponding color coded areas of both spaces. In the case of CYGNSS, a larger "full ddm" is formed spanning a total of 128 delay bins (half of which include measured signal while the other half is typically reserved for noise floor estimation) sampled at a ≈0.25 chip resolution and 20 Doppler bins sampled at 500 Hz with a 1 ms coherent integration and 500–1000 incoherent averages such that total integration time varies between 0.5–1 s. Subsequently, a smaller subset of pixels indicated in Fig. 2(b) is cropped, spanning a maximum of ≈3.5 chips, and downlinked for further ground processing; the latter
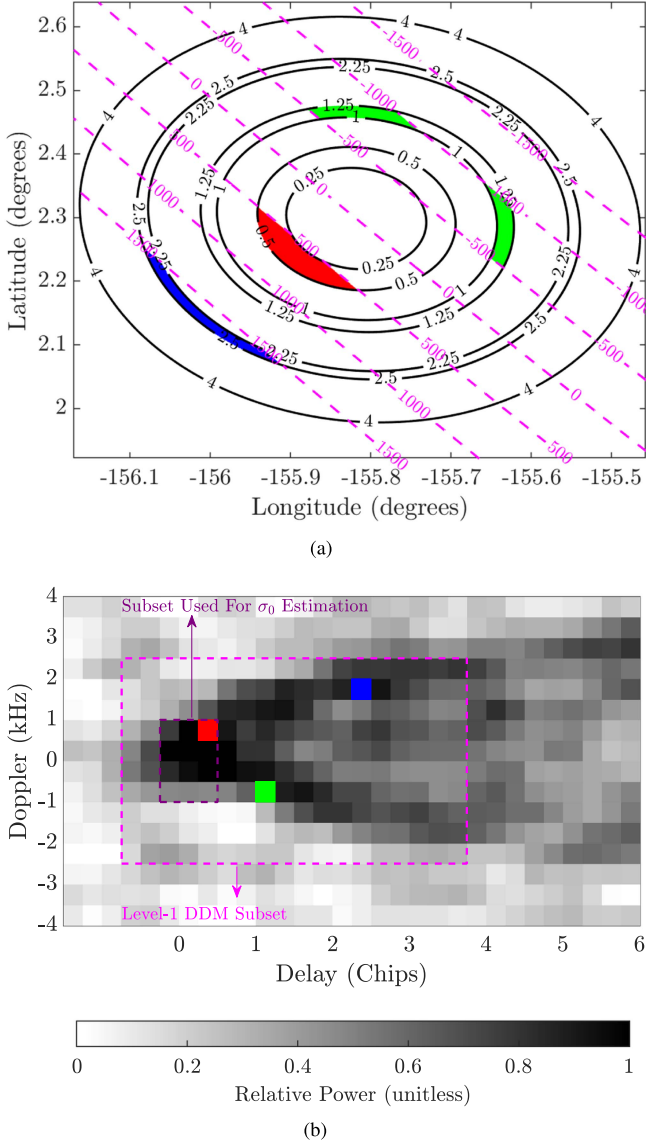
(a)

(b)

Fig. 2. Illustration of basic GNSS-R operating principle (a) Surface delay solutions in chips and Doppler in kHz solutions about the specular point. Constant delay ellipses are in black, constant Doppler hyperbolas are in magenta. 1 chip = 0.97 μs (b) Level-1 DDM. The partitioning of scattered power from the spatial domain to its delay/Doppler space bins is color coded. The example has been generated using the CYGNSS E2ES at Earth Centric Earth Fixed (ECEF) geometries corresponding to a 30.1 ° incidence angle assuming a flat Earth.

is the mission's standard "Level-1" DDM that is continuously available as part of the instruments' 100% duty cycle operation.

Power received for ocean surfaces sufficiently roughened by surface winds (with winds $\geq$ 5 m/s) may be described by the bistatic radar

$$P_R^{inc}(\tau,f) = \frac{P_T\lambda^2}{(4\pi)^3} \int_A \frac{G_T G_R(\tau,f)\sigma_0\Lambda^2(\tau-\tau')S^2(f-f')}{R_T^2(\tau,f)R_R^2(\tau,f)L_a}d\overline{A} \quad (1)$$

where P_R^{inc} is the incoherent component of received power at delay and Doppler offsets τ and f from the specular point describing random phase scattered field, P_T is the GNSS transmit power level, λ is the electromagnetic wavelength, σ_0 is

the surface NBRCS, G_T and G_R are the transmit and receive antenna pattern gains, respectively. The power decay with range on both the transmit and receive paths are accounted for using the respective range terms R_T and R_R with total atmospheric losses along the forward propagation path being accounted for through the L_a term. The product of the functions Λ and S are the delay and Doppler spreading functions.

Assuming sufficiently small footprints similar to those encountered with CYGNSS's Level-1 dataset, further simplifications to (1) can be made to derive observables like σ for use as part of standard Level-2 wind speed retrievals

$$\sigma = \frac{(4\pi)^3}{\lambda^2}\frac{1}{EIRP}\frac{P_R^{inc}R_T^2R_R^2L_a}{G_R} \quad (2)$$

such that the best available estimates for range losses, antenna gain dependencies, atmospheric losses, and varying levels of GNSS effective isotropic radiated power (EIRP) given by (3) are accounted for

$$EIRP = P_T \cdot G_T. \quad (3)$$

A smaller subset of pixels are selected for integration to form a delay Doppler map average (DDMA) that is later normalized by an equivalent effective scattering area DDM $\overline{A}$ to compute NBRCS

$$\sigma_0 = \frac{\sum_{i=-1}^{1}\sum_{j=-2}^{2}\sigma(\tau_T+i, f_T+j)}{\sum_{i=-1}^{1}\sum_{j=-2}^{2}\overline{A}(\tau_T+i, f_T+j)} \quad (4)$$

where τ_T and f_T are the specular bin (or tracking point) delay and Doppler indices, respectively.

Estimates of the scattering areas used as part of the normalization process may first be computed using forward models describing the total physical area $A(\tau,f)$ (5) satisfying the delay/Doppler limits for a given DDM pixel and later convolved with the Woodward Ambiguity function to describe the effective scattering area $\overline{A}(\tau, f)$ given by (6). The process is typically repeated for a wide range of receiver elevations, incidence angles, and azimuth rotation angles to form a reference scattering area look up table (LUT)

$$A(\tau,f) = \iint dxdy \quad (5)$$

$$\overline{A}(\tau,f) = \iint \Lambda^2(\tau-\tau')S^2(f-f')dxdy. \quad (6)$$

Much of the simplifications made in the case of CYGNSS's Level-1 DDMs hinge on the limited $\approx$0.5–0.75 chip delay extent of related observables, which enables reducing parameters like $G_R(\tau,f)$ to constants, which is not expected to be always generalizable to the larger $\approx$16 chip full DDMs as shown in the example in Fig. 3(a). In this example, a CYGNSS L1 Earth-Centric-Earth-Fixed (ECEF) observation geometry is used to project delay, Doppler, and gain contours onto the surface spanning a $\approx$300 km footprint. Subsequently, "receive antenna gain DDMs" are computed in Fig. 3(b). Both highlight significant gain variability which, in this example, can be up to $\pm$4 dB. Here it is important to note several algorithm design considerations including the fact that CYGNSS's DDMs are 2-D measurements
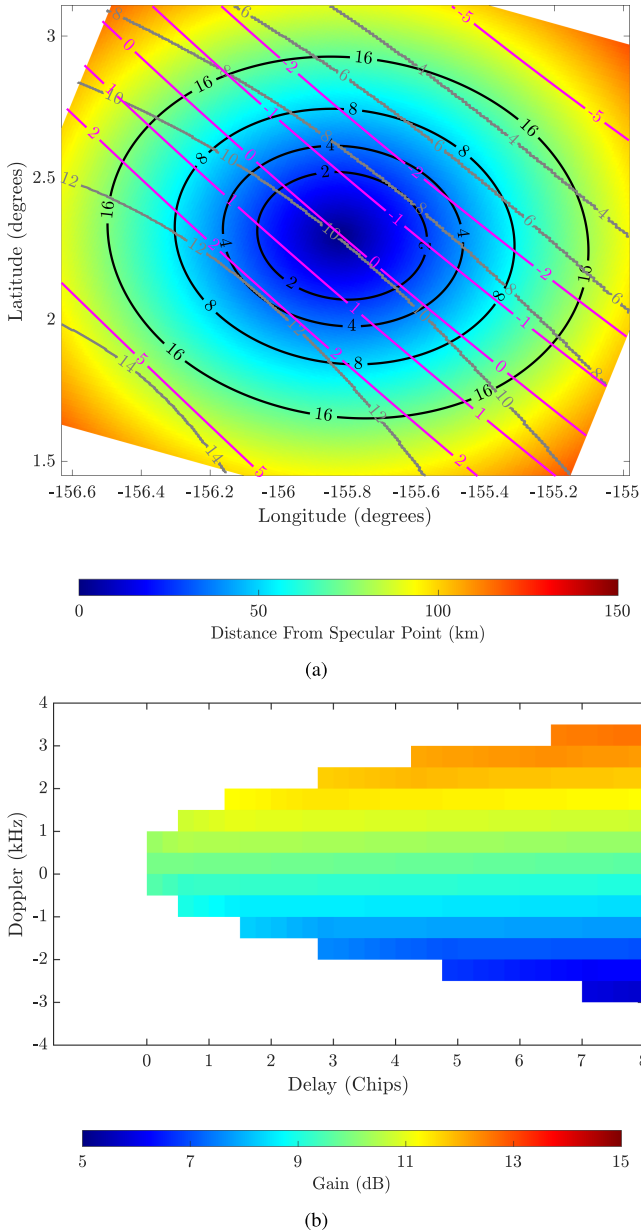
(a)

(b)

Fig. 3. Example CYGNSS observation scenario. (a) Constant delay in chips indicated by black contours, constant Doppler in kHz indicated by magenta contours, constant gain in dB indicated by gray contours. (b) Receive antenna gain projected onto delay/Doppler Space.
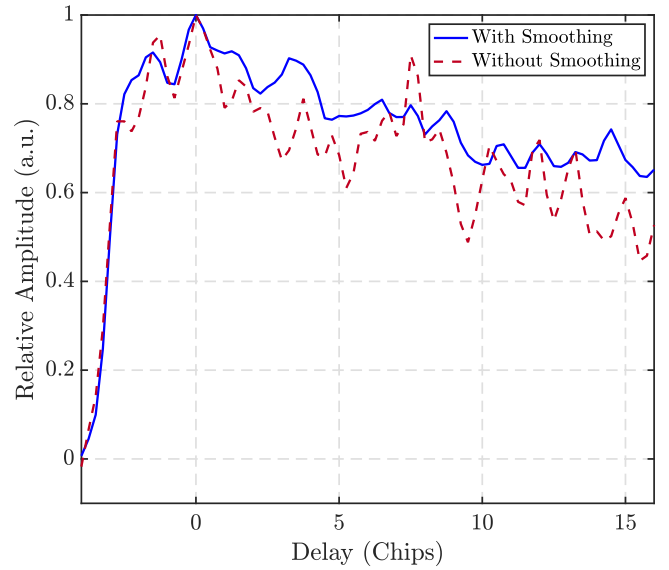

Fig. 4. Example CYGNSS power versus delay waveforms derived by integrating full DDMs along Doppler.
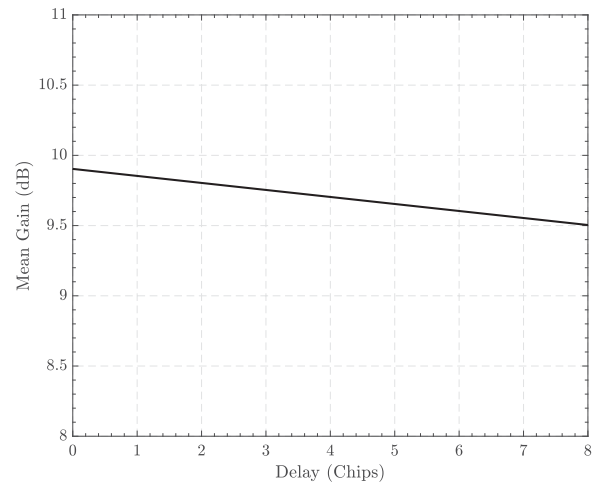

Fig. 5. Mean receive antenna gain versus delay using the example observation geometry shown in Fig. 3.

while the TES retrieval approach is concerned with using a 1-D power versus delay waveform. To derive the latter, the DDMs are integrated along Doppler. An example waveform is depicted in Fig. 4. In all the results that follow, a ±4 s moving averaging window is applied to full DDMs prior to deriving power versus delay waveforms and using them in subsequent retrievals. In addition, in this work retrieval attempts are limited to those with a receive gain on the order of 10 dB or greater. This both ensures that measurements retained for further analysis are of good quality but also partially mitigates the effects noted in Fig. 3. While gain can be lower on one side (positive or negative Dopplers), this is largely compensated for, when integrating the DDM along Doppler to generate the power versus delay

waveform, by the higher gains on the opposing side as depicted in Fig. 5 such that peak slope error due to this effect is limited to ≈ 5%. Closely related is the fact that retrieval attempts have shown that performance is optimized when maximum delay extent is limited to eight chips motivating using half of the full DDM's delay extent in the results that follow. This both ensures reduced gain driven slope related retrieval errors while also improving the retrievals spatial resolution. Nonetheless, given the ≈8 chip TES delay extent, compared to CYGNSS's Level-2 wind speeds being based on a ≈0.5–0.75 chip delay extent, the TES spatial resolution will inherently be significantly coarser.

B. Signal Processing and Related Properties

Reflection from the ocean surface is a stochastic process. As the ocean transitions from a flat surface under the influence of the wind, the wavelets begin to partition incoming power from the

first Fresnel zone and distribute it at longer delay paths. These longer delays come from areas where the wind slopes have the proper orientation to redirect the incoming microwave field in the direction of the satellite receiver.

Loci of constant delay can be shown to be represented by a family of ellipses, nearly perfectly concentric, whose semimajor and semi-minor axes are given by

$$a = \frac{\sqrt{2hc\tau}}{\sin^{\frac{3}{2}}\gamma} \tag{7}$$

$$b = \frac{\sqrt{2hc\tau}}{\sin^{\frac{1}{2}}\gamma} \tag{8}$$

where h is satellite height over the surface, c is speed of light, τ is the delay (excess over the bulk delay), and γ is the elevation angle in degrees. It is noted that (1-2), assuming a flat Earth, are used in this work for simplicity. As part of future investigations, the impacts of the Earth's curvature should be taken into account as they can be significant from spaceborne altitudes.

From [13], the received signal $I(\tau)$ after its transformation to polar coordinates from the surface can be approximated as being proportional to the integral:

$$I(\tau) = \frac{1}{\sigma_x \sigma_y} \int \Lambda^2(r, \phi, c \cdot \tau) e^{\frac{1}{2}\left(\frac{\tan^2 \beta_x}{\sigma_x^2} + \frac{\tan^2 \beta_y}{\sigma_y^2}\right)} r dr d\phi \tag{9}$$

where r is the radial separation from the specular point, ϕ is the azimuth angle, $\tan(\beta_x)$ and $\tan(\beta_y)$ are the x/y oriented tangent scattering vectors, Λ^2 is the temporal autocorrelation function of the GPS transmitted code, with the up/cross wind mean square slopes represented by σ_x^2 and σ_y^2, respectively. The signal acquired by the satellite receiver, after processing, consists of a surface integral of a bivariate Gaussian SPDF, given as

$$\text{SPDF} = \frac{\exp\left(-\frac{1}{2}\frac{\tan^2 \beta_x}{\sigma_x^2} + \frac{\tan^2 \beta_y}{\sigma_y^2}\right)}{2\pi\sigma_x\sigma_y} \tag{10}$$

where x and y are a surface coordinate system centered at the specular point.

This function is then integrated against the autocorrelation function Λ^2 associated with the selected satellite. The code comes from known copies in the receiver which are, in effect, then projected with varying controlled delays over the scattering surface. The code repeat cycle is such that a signal is produced every one millisecond. Improved signal to noise ratio is obtained by averaging.

The retrieval of ocean surface winds using CYGNSS's observables, namely NBRCS estimates, is facilitated by empirically based models [21] that relate these quantities to surface wind speeds using coincident model wind speed estimates. NBRCS is therefore inherently dependent on the form of the ocean's SPDF. In the bivariate slope probability function, the wind speed influence comes from the factors σ_x^2 and σ_y^2. Extensive aircraft flights into tropical cyclones have yielded a model mean squared slope (MSS) relationship for L-Band signals [14]

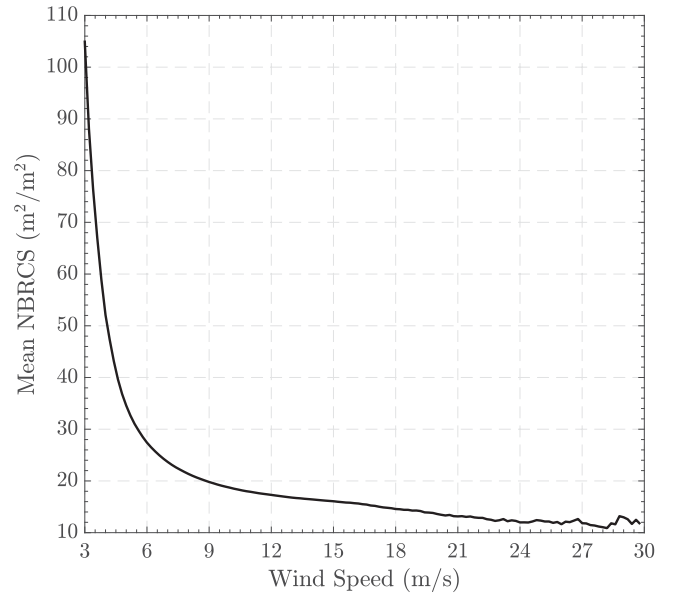$$\text{mss}_{\parallel} = 0.45 \cdot (0.000 + 0.00316 \cdot f(U)) \tag{11}$$

Fig. 6.   CYGNSS NBRCS binned by reference ECMWF surface winds.

$$\text{mss}_{\perp} = 0.45 \cdot (0.003 + 0.00192 \cdot f(U)) \tag{12}$$

where

$$f(U) = \begin{cases} U, & 0.0 < U \le 3.49 \text{ m/s} \\ 6 \cdot ln(U) - 4.0, & 3.49 < U \le 46.0 \text{ m/s} \\ 0.411 \cdot U, & U > 46.0 \text{ m/s} \end{cases}$$

where the MSS is defined to be perpendicular ($\text{mss}_{\parallel}$) to and along ($\text{mss}_{\perp}$) the wind direction. It is noted that other parametrizations of this relationship are available in the relevant literature [15]. Referring back to the bivariate SPDF (10), the value of this function at the specular point ($\beta_x = \beta_y = 0$) is inversely proportional to ($\sigma_x \cdot \sigma_y$). In other words, the reflected power from in and around the specular point is inversely proportional to the wind speed. Accurate calibration of the GPS reflections therefore facilitate wind speed retrievals. An example of receive power decay as a function of surface winds using a multiyear CYGNSS data record is depicted in Fig. 6, where a clear correlation of CYGNSS's measurements to wind speeds is observed and evidenced by the NBRCS's monotonic decay.

In spite of the continued improvement of the quality of CYGNSS's baseline Level-2 wind speed retrievals over the mission's consecutive data releases, it is important to acknowledge the calibration challenges associated with the use of GNSS-R systems' observables which in turn can compromise the quality of retrievals [22], [23], [24], [25], [26]. In the case of CYGNSS, the uniqueness related challenges derive from the fact that each of its two, port and starboard, receive channels are capable of tracking four reflections simultaneously such that a total of 32 DDMs may be formed over a given integration period with minor FM/channel specific biases potentially compromising the quality of the calibration applied to Level-1 DDMs. This is further compounded by the facts that specularly reflected transmissions originate from GPS space vehicles whose properties are not fully characterized and can change over time. EIRP "flexing"

for example has been a challenge of particular note. This is further compounded by the dynamic external noise environment CYGNSS operates in where recent investigations have shown that interference from L-band GNSS augmentation systems can lead to a clear geospatial dependence of noise floor estimates, which can ultimately offset derived NRBCS estimates at the $12 \text{ m}^2/\text{m}^2$ level (52% relative to the CYGNSS mean) if not adequately accounted for [23], [24]. The effects of such challenges become more acute at higher wind speeds, where the MSS has a much weaker, logarithmic, response motivating complementing standard retrieval approaches with techniques that may be less sensitive to some of these calibration uncertainties.

C. Trailing Edge Slope Method

In Section II-B, the form of the slope probability density was presented as a bivariate Gaussian with mean square slope appearing in two places, as a multiplicative factor and as a factor in the exponential. As previously noted, CYGNSS's standard Level-1 DDM comprises data over a range of delays, the normal set is 17 delay bins of one quarter chip each, and 11 Doppler bins. This set begins below the advent of data and continues to two chips into the expected surface delay. Such a setting takes into account the fact that there may be error in calculating bulk delay to surface as well as a necessity to capture all the power from around the specular point. To address the suitability of these standard Level-1 DDMs for TES retrievals, particularly at higher winds, it is noted that from the form of the Gaussian convolved with the autocorrelation function, it is required that the delay range cover two full code chips to reach maximum returned signal. To illustrate this, we note that the $\tan^2(\beta_x)$ and $\tan^2(\beta_y)$ factors are the scattering angles from the incoming GPS surface signal to the receivers. They can be expressed near the specular point as

$$\tan^2(\beta_x) \cong \frac{(r\cos\phi)^2}{(2h)^2} \tag{13}$$

$$\tan^2(\beta_y) \cong \frac{(r\sin\phi)^2}{(2h)^2} \tag{14}$$

where x and y are now expressed in a polar coordinate system centered on the specular point. Making a change of variables $x \cdot \sin(\gamma) = x'$ converts the elliptical loci of constant range into circles and simplifies the surface integration. For a wind speed of one meter per second, the MSS is on the order of 1.0×10^{-3}. The $1/e$ point for the Gaussian can be found to be approximately 50 km. Since virtually all wind speeds are higher than one meter per second (0.5 knots), the $1/e$ point is always outside the range bins.

Expanding the Gaussian in its first terms in β is therefore warranted. Doing this gives

$$K \cdot \left(1 - \frac{1}{2} \cdot \left(\left(\frac{1}{\sigma_\perp^2}\right) \cdot \left(\frac{r'\cos\phi}{\sin(\gamma)}\right)^2 \right. \right.$$
$$\left. \left. + \left(\frac{1}{\sigma_\parallel^2}\right) \cdot (r'\sin\phi)^2\right) \cdot \left(\frac{1}{2h}\right)^2\right). \tag{15}$$

Integration over ϕ gives

$$K \cdot \left(1 - \frac{1}{4} \cdot r'^2 \left(\left(\frac{1}{\sigma_\perp^2}\right) \cdot \left(\frac{1}{\sin(\gamma)}\right)^2 \right. \right.$$
$$\left. \left. + \left(\frac{1}{\sigma_\parallel^2}\right)\right) \cdot \left(\frac{1}{2h}\right)^2\right). \tag{16}$$

With regard to the MSS, there is at present no demonstration of an anisotropy in up-wind-down-wind versus cross-wind MSS. For this reason, an isotropic value σ_I^2 is assumed for $\sigma_\perp^2$ and $\sigma_\parallel^2$.

Moving on to expressing the surface radii of constant delay in terms of code delay setting τ, the (scaled) radius r' is

$$r' = \sqrt{2 \cdot h \cdot \sin(\gamma) \cdot c \cdot \tau} \tag{17}$$

with c speed of light and h spacecraft height

$$K \cdot \left(1 - \frac{1}{2} \cdot h \cdot \sin(\gamma) \cdot c \right.$$
$$\left. \cdot \tau \cdot \frac{1}{\sigma_I^2} \cdot \left(\left(\frac{1}{\sin(\gamma)}\right)^2 + 1\right) \cdot \left(\frac{1}{2h}\right)^2\right) \tag{18}$$

where K contains all the factors of amplifier gain, antenna effects, MSS factors, GPS illumination power, etc. It is also the value of signal at the specular point as can be seen by setting the delay to zero. The remaining factors in the calculation of slope are available from instrument-calculated parameters as seen in (12). The start bin can be any range bin past the full development of signal. The actual peak signal occurs at two chips after the first onset of signal such that measurements with a longer delay extent would be better suited for related analyses. This is a result of the convolution of the lambda-squared function with the slope probability function, which is zero at delays before the bulk range delay is surpassed. The SPDF near zero slope is constant, causing the developed signal to increase until a prescribed number of delay τ_0 chips are encompassed.

Any other range bin can be chosen as the start of the slope determination. It should be noted that the use of other than the specular point range bin degrades surface resolution. Removing the various system effects mentioned above is done by making use of the extended range bins as follows:

1) The slope of the data from close to the first data-containing range/Doppler bins ("start bin") out to some practical maximum. Change in signal over a number of bins divided by number of bins;
2) this is then divided by the value from the start bin. The unknown constants now disappear; and
3) wind speed is determined by comparing the ideal slope ν (and known constants) to the measured slope via the experimentally determined MSS relationship:

$$\nu = \frac{K \cdot \frac{1}{2} \cdot h \cdot \sin\gamma \cdot c \cdot \tau_0 \frac{1}{\sigma_I^2} \cdot \left(\frac{1}{\sin^2\gamma} + 1\right) \cdot \left(\frac{1}{2h}\right)^2}{K \cdot \frac{1}{2} \cdot h \cdot \sin\gamma \cdot c \cdot \tau_0 \cdot \left(\frac{1}{\sin^2\gamma} + 1\right) \cdot \left(\frac{1}{2h}\right)^2} \approx \frac{1}{\sigma_I^2}. \tag{19}$$
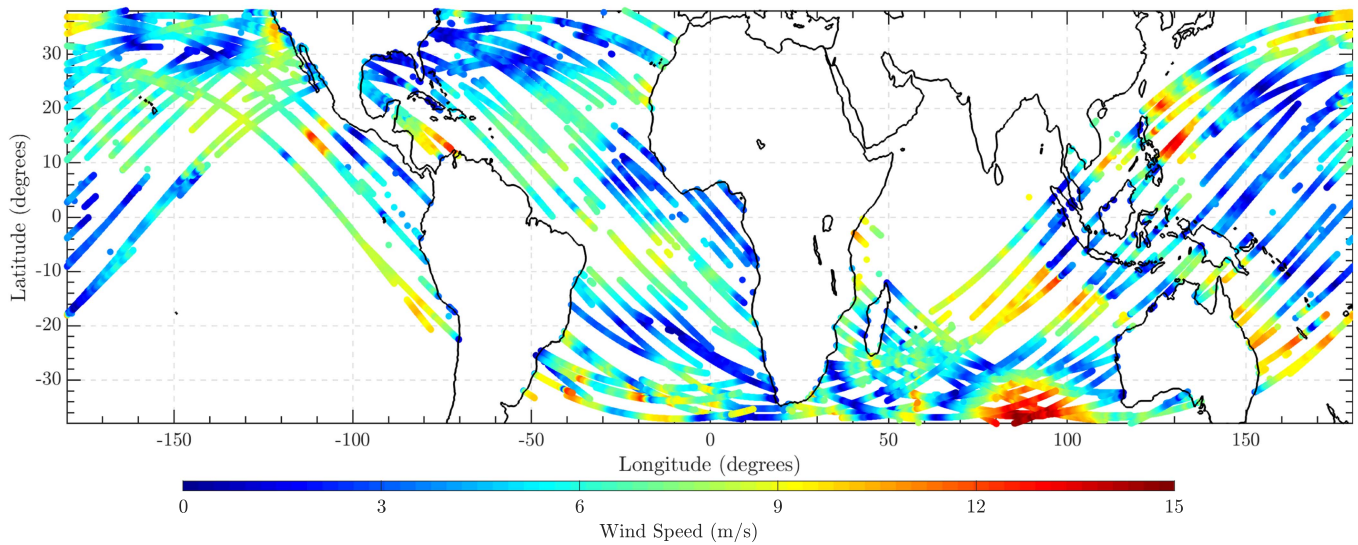
Fig. 7. Distribution of specular points where CYG08 was commanded to conduct full ddm collections for a period of ≈9 h starting DOY 158 (June 7th), 2018 color coded by reference ERA-5 wind speeds spatially and temporally interpolated to CYGNSS's observation times and locations.
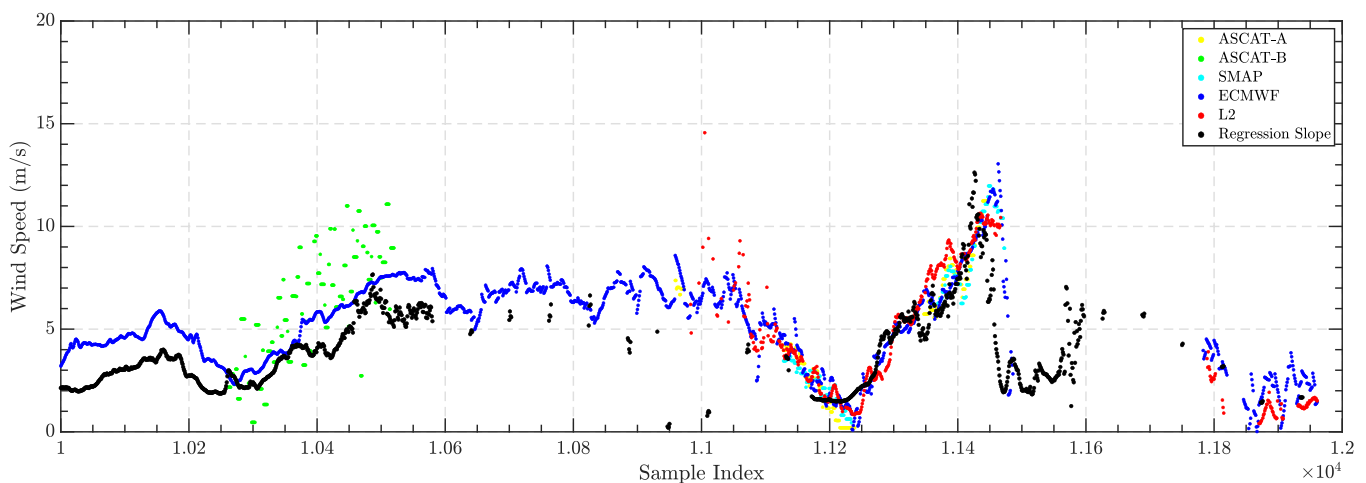

Fig. 8. Time series of retrieved surface winds using TES approach for track observing Hurricane Aletta an east Pacific storm off Baja, California. To provide context for the temporal behaviors the retrieval results are contrasted with observations from AScat-A, AScat-B, SMAP, ECMWF, and CYGNSS's standard L2 estimates.

Or, including noise $\mathcal{N}$ in the data measurement:

$$\frac{1}{\sigma_I^2} = \frac{SignalValue(\tau = 0) - SignalValue(\tau = \tau_0)}{SignalValue(\tau = 0) \cdot SignalValue(\tau = \tau_0)} + \mathcal{N}. \tag{20}$$

Added noise contaminates the slope calculation. The estimated slope in the presence of noise can be determined by a simple last minus first, or using a best fit such as least square. Another method is to use the complete recorded power versus delay, which includes the autocorrelation function as input to a matched filter, yielding an optimum fitting to model wave forms. All three have been implemented for this article and will be presented. Because this method uses the "tail" of the acquired data, it is referred to as the trailing edge slope method or TES method. It is important to note: No calibration at all is required by this method.

III. RESULTS

Given the need for downlinks with longer delay extents, the utility of trailing edge slope retrievals together with the proposed formulation was explored in the context of a special CYGNSS "full ddm" downlink extending ≈9 h on DOY 158, 2018. The continuous collection by CYG08 has enabled the sampling of up to ≈100 000 ocean points with a variety of surface conditions depicted in Fig. 7. To highlight the efficacy of the proposed approach, a time series of measurements coinciding with Hurricane Aletta, an east Pacific storm off Baja, California is depicted in Fig. 8. Multiple sources for reference winds were assembled to provide context for the observed trends including CYGNSS baseline retrieval (L2) along with colocated ASCAT-A, ASCAT-B scatterometers, and soil moisture active passive (SMAP) results.

TABLE I
STATISTICAL MEASURES USING ECMWF AS TRUTH

	Simple Slope	Regression	Matched Filter
$A \cdot x$ Fit	0.945	0.963	0.995
A Fit STD	0.285%	0.292%	0.423%
W.S. STD	2.133	2.229	3.341

TABLE II
STATISTICAL MEASURES USING GDAS AS TRUTH

	Simple Slope	Regression	Matched Filter
$A \cdot x$ Fit	0.963	0.963	1.025
A Fit STD	0.310%	0.291%	0.351%
W.S. STD	2.304	2.395	3.801

TABLE III
WIND SPEED STD AND POINTS GAIN 0F $G_R \geq 12$

Reference	TES STD, $G_R \geq 12$	Points, $G_R \geq 12$
ECMWF	2.158	16901
GDAS	2.309	16923
CYGNSS L2	2.301	8430

TABLE IV
WIND SPEED STD AND POINTS GAIN 0F $G_R \geq 10$

Reference	TES STD, $G_R \geq 10$	Points, $G_R \geq 10$
ECMWF	3.415	29946
GDAS	3.599	29970
CYGNSS L2	3.194	15969

To provide a more comprehensive statistical analysis of anticipated retrieval performance, the TES approach was extended to all available ocean measurements with sufficiently high antenna gain ($G_R \geq 12$). The enforcement of a minimum gain requirement is motivated by the fact that the TES retrieval approach is fundamentally a waveform shape measure whose retrievals will be impacted by noisy observations whose shapes are distorted. The appropriate scale factors for model versus measurements TES fits determined using matchups to two independent datasets are summarized in Tables I and II, respectively. Additional wind speed and measurement density statistics are summarized in Tables III and IV.

A direct calculation of sample standard deviation was also done for the entire Day 158, 2018. Selection conditions are that the gain was at or above 12 (11 dB) and 10 (10 dB), which corresponds to elevation angle and azimuth direction approximately $60°$ and/or $90 (270)°$ relative to spacecraft translation direction. The choice of two antenna gain increments is intended to highlight considerations relating to measurement quality versus sample density tradeoffs. In addition, limiting the pool of measurements in future analyses to portions of the receive antenna pattern, where the rate of gain change as a function of incidence angle is limited (i.e., main lobe) may aid in improving the quality of the retrievals.

Wind speed for GDAS varied from 0 to 20.4 m/s with an average of 4.4 m/s, while ECMWF values ranged from 0 to 15.9 m/s with an average of 4.6 m/s. The standard deviation of CYGNSS L2 retrievals against ECMWF wind speed was found to be 2.05495 m/s with 42 658 reported points out of 93 961. Slightly elevated error statistics were observed when using GDAS as truth.

IV. DISCUSSION

The success of the TES retrieval methodology is evidenced by the high correlation of related retrievals to a variety of independent reference datasets. Given the fact that standard L2 retrievals are subject to a variety of calibration related considerations, it is observed that for up to 50% of the data where TES retrievals are attempted no corresponding L2 wind speed estimate is available.

It is nonetheless acknowledged that the proposed approach provides estimates of a coarse resolution. The data reported here utilizes 32 one-quarter chip steps (eight whole chips) of data, yielding surface coverage 134 by 106 km. Improved surface resolution can be accomplished by reducing the number of chips. Since the surface-reflected signal noise is Rayleigh distributed, a single measurement signal-to-noise would be near unity or less. Adding uncorrelated noise together increases the signal-to-noise. However, the "signal" depends on the number of chips as well and reducing the number of chips gives the slope error dependent on the same individual noise samples as before but with less signal change. The retrieval error would increase as surface resolution is increased.

The greatest addition to error and limitation of accuracy comes from the actual nonconstant slope as the antenna more radically affects the form of the received power versus delay signal. While the antenna gain pattern is known as well as orientation with respect to the spacecraft, the use of higher order corrections was not considered here. The fundamental benefit to the trailing slope method comes not from the simplicity of the linear slope, but from the removal of unknown and changing conditions on calibration. Taking into effect the antenna gain requires a power versus delay normalized functional relationship (e.g., polynomial) that expresses the antenna effect on the power versus delay. In principle, this would then be fitted to the acquired data with the error minimized in some fashion. It is to be expected that utilizing this information would enhance TES by allowing retrievals in the more general case found in the orientation of the transmitting GPS satellite to the CYGNSS receiving satellite.

V. CONCLUSION

Retrieving wind speed from satellite altitude can be done by monitoring the reflected GPS power received at a satellite by means of end-to-end, microwave radiometric calibration. This requires considerable and continuing effort, with several opportunities for error: GPS transmitted power must be determined, the distribution of the power on the surface must be known, the receiving antenna pattern, the receiver electronic gain among others must be known. These are functions of time, under the influence of changing GPS satellites, receiving satellite

orientation, even receiver system temperature. An alternative method for retrieval, the trailing edge slope (TES) method of wind speed retrieval of data from the CYGNSS space mission has been presented here along with results taken from data acquired in June of 2018. Results presented here show that the TES method produces results comparable with the standard CYGNSS wind speed product under some fairly broad conditions. The TES method requires additional data downlink of power-versus-delay over the baseline CYGNSS method. Surface resolution is degraded. At the very least, the TES method offers a powerful monitor for the baseline CYGNSS approach. Since the method is inherently very simple, at least for the high gain-linear conditions, on board processing of the retrieval could be done in very simple, fixed hardware (firmware) and downlinked at a relatively low rate. Enhancements were also discussed to expand the conditions of applicability of the method.

REFERENCES

[1] S. Sternberg and A. Schnapf, "Performance and evaluation of satellites Tiros I and Tiros II," *ARS J.*, vol. 31, no. 11, pp. 1495–1505, 1961, doi: 10.2514/8.5838.

[2] A. Bentamy, D. Croize-Fillon, and C. Perigaud, "Characterization of ASCAT measurements based on buoy and QuikSCAT wind vector observations," *Ocean Sci.*, vol. 4, pp. 265–274, 2008, doi: 10.5194/osd-5-77-2008.

[3] L. Ricciardulli, "ASCAT on metOp-A data product update notes," RSS, Tech. Rep. 040416, 2016, doi: 10.56236/rss-bb.

[4] W. Ni, A. Stoffelen, K. Ren, X. Yang, and J. Vogelzang, "SAR and ASCAT tropical cyclone wind speed reconciliation," *Remote Sens.*, vol. 14, no. 21, 2022, Art. no. 5535, doi: 10.3390/rs14215535.

[5] M. Martín-Neira, "A passive reflectometry and interferometry system (PARIS): Application to ocean altimetry," *ESA J.*, vol. 17, pp. 331–355, 1993.

[6] S. J. Katzberg and J. Garrison, "Utilizing GPS to determine ionospheric delay over the ocean," NASA, Washington, DC, USA, Tech, Memorandum NASA-TM-4750, Dec. 1996.

[7] V. U. Zavorotny and A. G. Voronovich, "Scattering of GPS signals from the ocean with wind remote sensing application," *IEEE Trans. Geosci. Remote Sens.*, vol. 38, no. 2, pp. 951–964, Mar. 2000.

[8] A. G. Voronovich and V. U. Zavorotny, "Bistatic radar equation for signals of opportunity revisited," *IEEE Trans. Geosci. Remote Sens.*, vol. 56, no. 3, pp. 1959–1968, Apr. 2018.

[9] M. M. Al-Khaldi, A. Bringer, and J. T. Johnson, "Studies of a rapid change detector using CYGNSS Level-2 wind speed products," *IEEE J. Sel. Topics Appl. Earth Observ. Remote Sens.*, vol. 14, pp. 7931–7937, 2021.

[10] R. Balasubramaniam and C. Ruf, "Characterization of rain impact on L-band GNSS-R ocean surface measurements," *Remote Sens. Environ.*, vol. 239, 2020, Art. no. 111607.

[11] C. S. Ruf et al., "Cyclone global navigation satellite system," Michigan Publishing, Univ. Michigan, Ann Arbor, MI, USA, 2022.

[12] C. S. Ruf et al., "New ocean winds satellite mission to probe hurricanes and tropical convection," *Bull. Amer. Meteorol. Soc.*, vol. 97, no. 3, pp. 385–395, 2016.

[13] S. J. Katzberg, J. Dunion, and G. G. Ganoe, "The use of reflected GPS signals to retrieve ocean surface wind speeds in tropical cyclones," *Radio Sci.*, vol. 48, no. 4, pp. 371–387, Jul. 2013, doi: 10.1002/rds.20042.

[14] S. J. Katzberg, O. Torres, and G. Ganoe, "Calibration of reflected GPS for tropical storm wind speed retrievals," *Geophysical Res. Lett.*, vol. 33, Sep. 2006, Art. no. L18602, doi: 10.1029/2006GL026825.

[15] P. A. Hwang and Y. Fan, "Low-frequency mean square slopes and dominant wave spectral properties: Toward tropical cyclone remote sensing," *IEEE Trans. Geosci. Remote Sens.*, vol. 56, no. 12, pp. 7359–7368, Dec. 2018.

[16] S. Gleason et al., "Study of surface wind and mean square slope correlation in hurricane like with multiple sensors," *IEEE J. Sel. Topics Appl. Earth Observ. Remote Sens.*, vol. 11, no. 6, pp. 1975–1988, Jun. 2018, doi: 10.1109/jstars.2018.2827045.

[17] E. Cardellach et al., "Mediterranean balloon experiment: Ocean wind speed sensing from the stratosphere, using GPS reflections," *Remote Sens. Environ.*, vol. 88, no. 3, pp. 351–362, 2003, doi: 10.1016/s0034-4257(03)00176-7.

[18] J. L. Garrison, A. Komjathy, V. U. Zavorotny, and S. J. Katzberg, "Wind speed measurement using forward scattered GPS signals," *IEEE Trans. Geosci. Remote Sens.*, vol. 40, no. 1, pp. 50–65, Jan. 2002, doi: 10.1109/36.981349.

[19] M. P. Clarizia, C. S. Ruf, P. Jales, and C. Gommenginger, "Spaceborne GNSS-R minimum variance wind speed estimator," *IEEE Trans. Geosci. Remote Sens.*, vol. 52, no. 11, pp. 6829–6843, Nov. 2014.

[20] M. P. Clarizia and C. S. Ruf, "On the spatial resolution of GNSS reflectometry," *IEEE Geosci. Remote Sens. Lett.*, vol. 13, no. 8, pp. 1064–1068, Aug. 2016.

[21] C. S. Ruf and R. Balasubramaniam, "Development of the CYGNSS geophysical model function for wind speed," *IEEE J. Sel. Topics Appl. Earth Observ. Remote Sens.*, vol. 12, no. 1, pp. 66–77, Jan. 2018, doi: 10.1109/JS-TARS.2018.2833075.

[22] S. Gleason, C. S. Ruf, A. J. O'Brien, and D. S. McKague, "The CYGNSS level 1 calibration algorithm and error analysis based on on-orbit measurements," *IEEE J. Sel. Topics Appl. Earth Observ. Remote Sens.*, vol. 12, no. 1, pp. 37–49, Jan. 2019.

[23] S. Gleason, J. Johnson, C. Ruf, and C. Bussy-Virat, "Characterizing background signals and noise in spaceborne GNSS reflection ocean observations," *IEEE Geosci. Remote Sens. Lett.*, vol. 17, no. 4, pp. 587–591, Apr. 2020.

[24] S. Gleason, M. M. Al-Khaldi, C. S. Ruf, D. S. McKague, T. Wang, and A. Russel, "Characterizing and mitigating digital sampling effects on the CYGNSS level 1 calibration," *IEEE Trans. Geosci. Remote Sens.*, vol. 60, 2022, Art. no. 5802812.

[25] T. Wang, C. S. Ruf, B. Block, D. S. McKague, and S. Gleason, "Design and performance of a GPS constellation power monitor system for improved CYGNSS L1B calibration," *IEEE J. Sel. Topics Appl. Earth Observ. Remote Sens.*, vol. 12, no. 1, pp. 26–36, Jan. 2019.

[26] T. Wang et al., "Dynamic calibration of GPS effective isotropic radiated power for GNSS-reflectometry earth remote sensing," *IEEE Trans. Geosci. Remote Sens.*, vol. 60, 2022, Art. no. 5800512.

Stephen J. Katzberg was born in Clinton, SC, USA, in 1943. He received the B.S. degree in electrical engineering from Massachusetts Institute of Technology, Cambridge, MA, USA, in 1965, and the M.S. and Ph.D. degrees in electrical engineering from the University of Virginia, Charlottesville, VA, USA, in 1967 and 1970, respectively.

He worked nearly exclusively with NASA Langley Research Center for 40 some-odd years, and is currently a Distinguished Research Associate with Langley, VA, USA, and an Adjunct Professor with South Carolina State University, Orangeburg, SC, USA.

Mohammad M. Al-Khaldi (Member, IEEE) received the bachelor's degree in electrical engineering from the American University of Sharjah, Sharjah, UAE, in 2015, the M.S. degree in electrical engineering from Texas A&M University, College Station, TX, USA, in 2017, and the M.S. degree in electrical and computer engineering from The Ohio State University, Columbus, OH, USA, in 2019, where he received the Ph.D. degree with the Department of Electrical and Computer Engineering, ElectroScience Laboratory, Columbus, OH, USA, in 2020.

He was previously a Project Scientist I, Postdoctoral Fellow II, and Postdoctoral Fellow I with the University Corporation for Atmospheric Research's COSMIC Program in Boulder, CO, USA. He is currently a Senior Research Associate with The Ohio State University's ElectroScience Laboratory and Department of Electrical and Computer Engineering. He is a member of the NASA CYGNSS mission science team, NASA CYGNSS mission calibration and validation team, IEEE GRSS Technical Committee on Modeling in Remote Sensing, IEEE GRSS Technical Committees on Frequency Allocations in Remote Sensing, is an associate member of commissions B and F of the International Union of Radio Science, is a NASA CSDA GNSS-R Subject Matter Expert, and serves as an Associate Editor of Radio Science. His current research interests include applied electromagnetics, rough surface scattering, and spaceborne remote sensing.

Faozi Said received the M.Sc. degree in electrical engineering from Brigham Young University, Provo, UT, USA, in 2009, and the Ph.D. degree in physics from the University of Tromsø, Tromsø, Norway, in 2015.

From 2012 to 2014, he was a Guest Research Scientist with the Spatial Oceanography Laboratory, French Research Institute for Exploitation of the Sea, Brest, France. He is working for Global Science and Technology, Inc., Greenbelt, MD, USA, as a Senior Research Scientist with the Ocean Surface Winds Team, Center for Satellite Application and Research, National Environmental Satellite Data and Information Service, National Oceanic and Atmospheric Administration. His research interests include sea surface wind retrieval algorithm development for both active and passive microwave remote sensing instruments, including the Scatsat-1 and NASA Cyclone Global Navigation Satellite System missions. His work also includes data calibration and validation of these two missions, including the SMAP satellite mission.

Jeonghwan Park (Member, IEEE) received the B.S. degree in electrical engineering from Yonsei University, Seoul, South Korea, in 2006, and the M.S. degree in electrical engineering from the Korea Advanced Institute of Science and Technology, Daejeon, South Korea, in 2008, and the Ph.D. degree from the Department of Electrical and Computer Engineering and ElectroScience Laboratory, The Ohio State University, Columbus, OH, USA, in 2017.

He has been working for Global Science and Technology, Inc., Greenbelt, MD, USA, as a Support Scientist I/II. In 2018, he joined the Ocean Surface Winds Team with the Center for Satellite Application and Research, National Environmental Satellite Data and Information Service, National Oceanic and Atmospheric Administration, College Park, MD, USA. Since 2020, he has been working with the Hydrological Science Laboratory, NASA Goddard Space Flight Center, Greenbelt, MD, USA. His research interests include satellite data calibration and validation, GNSS-R remote sensing applications, and active microwave remote sensing for soil moisture applications.